Modeling of Casting, Welding, and Advanced Solidification Processes VIII, B.G. Thomas and C. Beckermann, eds.,
(San Diego, CA, June 7-12, 1998), TMS, Warrendale, PA, 1998, pp. 1185-1199; [Best Experimental Paper Award, 1998, MCWASP VIII]

MEASUREMENT OF TEMPERATURE, SOLIDIFICATION, AND MICROSTRUCTURE IN A CONTINUOUS CAST THIN SLAB

B. G. Thomas*, R. O'Malley++, and D. Stone*

*Department of Mechanical and Industrial Engineering
University of Illinois at Urbana-Champaign
1206 West Green Street, Urbana, IL 61801
Ph: 217-333-6919; Fax: 217-244-6534; email: bgthomas@uiuc.edu

++ARMCO Research and Technology
705 Curtis Street,
Middletown, Ohio 45044
Ph: 513-727-5708; Fax: 513-727-5872; email: OMalleyRJ@armco.com

Abstract

Experiments have been conducted to quantify shell growth, heat transfer and microstructure during the continuous casting of 132 mm-thick stainless-steel slabs at the ARMCO Inc. caster in Mansfield, OH. A breakout shell was obtained and the shell thickness profile is measured down several vertical lines around the shell perimeter. A complete documentation is provided of the mold geometry, casting conditions, and derived solidification time as a function of distance down the breakout shell. Mold temperatures and cooling water temperature increase were measured for similar casting conditions using a mold instrumented with 106 thermocouples. Microstructures are presented which show the dendrites and both primary and secondary arm spacing measurements are included. The final grain structure is presented for several different macro-etched sections. These experimental measurements should be of use in the calibration and validation of mathematical models of continuous casting.

Modeling of Casting, Welding, and Advanced Solidification Processes VIII, B.G. Thomas and C. Beckermann, eds.,
(San Diego, CA, June 7-12, 1998), TMS, Warrendale, PA, 1998, pp. 1185-1199; [Best Experimental Paper Award, 1998, MCWASP VIII]

Introduction

The continuous casting process is used to transform over 400 million tonnes of molten steel into semifinished slabs each year. To further improve quality and decrease cost, a quantitative fundamental understanding of heat transfer in this process is essential. Despite its importance, relatively few complete sets of experimental data have been published for the development and calibration of mathematical models.

This paper presents experimental measurements which were conducted to quantify shell growth, heat transfer, and microstructure at the Armco, Inc. stainless-steel thin-slab caster in Mansfield, OH. This caster was constructed by Voest Alpine and has been producing 100% direct-charge slabs since in 1995. Specifically, this paper reports the shell thickness profiles measured on a breakout that occurred on March 25, 1997. In addition to providing the relevant mold geometry and casting conditions, this paper includes mold temperatures and cooling water temperature increases measured under similar conditions. This data enables global heat flux calculations and is being used for the calibration of a detailed heat transfer model, CON1D, which is being developed at the University of Illinois [1]. Finally, etched sections are presented that reveal the dendrite arm spacings and as-cast grain macrostructure for use in future structure modeling.

General Process Description

Figure 1 illustrates the continuous-casting process for thin steel slabs. Molten steel flows through from a ladle, through the tundish, and into the mold through a "submerged entry nozzle", or SEN. Once in the mold, the molten steel freezes against the water-cooled copper mold walls to form a solid shell. Drive rolls lower in the machine continuously withdraw the shell from the mold at a "casting speed" that matches the flow of incoming metal, so the process ideally runs in steady state. The liquid level is maintained at a set distance below the top of the mold by a feed-back controller that adjusts the vertical position of the stopper rod in the tundish.

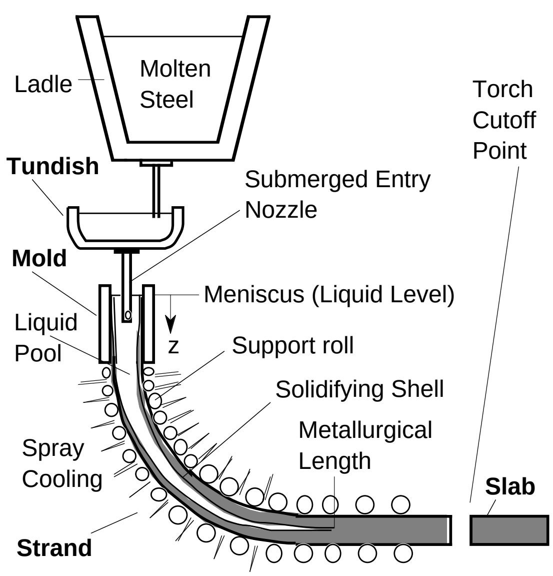

Figure 1 - Schematic of continuous casting process

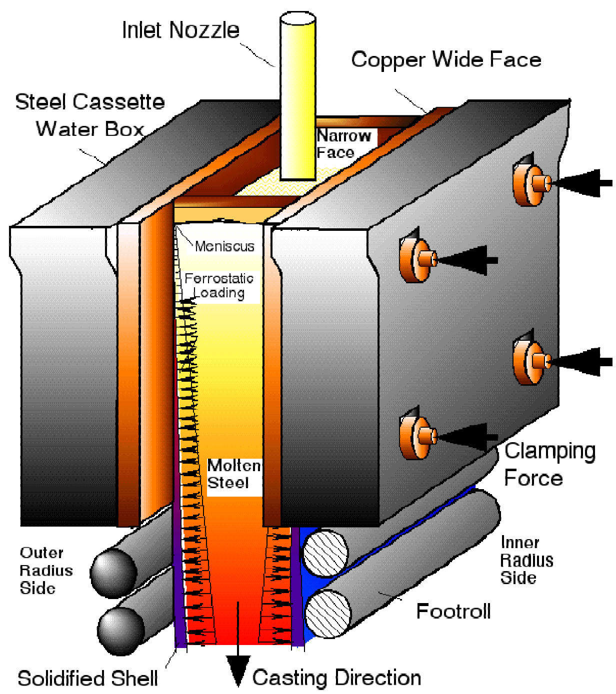

Figure 2 - Cutaway view of continuous casting mold showing narrow faces and wide faces (inner and outer radius), and solidifying shell

Modeling of Casting, Welding, and Advanced Solidification Processes VIII, B.G. Thomas and C. Beckermann, eds.,
(San Diego, CA, June 7-12, 1998), TMS, Warrendale, PA, 1998, pp. 1185-1199; [Best Experimental Paper Award, 1998, MCWASP VIII]

Below mold exit, the solidifying steel shell acts as a container to support the remaining liquid. Rolls support the steel shell to minimize bulging due to the ferrostatic pressure loading. Water and air mist sprays cool the surface of the strand between the rolls to maintain the steel surface temperature until the molten core is solid. After the center is completely solid, (at the "metallurgical length"), the strand can be torch cut into slabs.

Most of the important phenomena occur in the mold, pictured in Fig. 2. The mold is constructed of four independent walls. Movement of the "narrow faces", NF, allows casting of arbitrary widths. The "wide face", WF, on the outside radius is "fixed" rigidly to a solid steel anchoring frame. Clamping forces are applied to the inside radius wide face ("loose side") to balance the ferrostatic pressure which is transmitted from the molten steel cavity through the solidifying shell. Cooling water flows through vertical slots machined into the back of the copper mold walls, which are bolted to a steel water boxes act as a reservoir for the water, in addition to providing rigidity to minimize mold distortion.

The continuous casting process is subject to a variety of quality problems, including inclusion entrainment and cracks, both internal and on the surface. The most severe problem is a costly "break-out", where molten steel bursts through the shell. This is most likely to occur if heat transfer across the gap between the shell and the mold shell is insufficient to accommodate the superheat delivered to the inside of the solidifying shell, resulting in local thin regions of the shell that are unable to support the ferrostatic pressure.

Mold and Nozzle Geometry

The mold construction and water slot dimensions are shown in Figs. 3 - 5 and further geometry details are given in Table 1. The walls of the copper plates are straight (no curvature). The mold copper is C181 (Cr-Zr-Cu alloy) and the plate surfaces are coated with a uniform 0.1 mm thick layer of Chromium over a layer of Nickel tapered from 1 mm thick at mold top to 1.5 mm thick at mold bottom. The coatings are not shown in Figs. 3-5. The copper plates include welded studs, which are bolted to a 100 mm thick cassette-type steel water box.

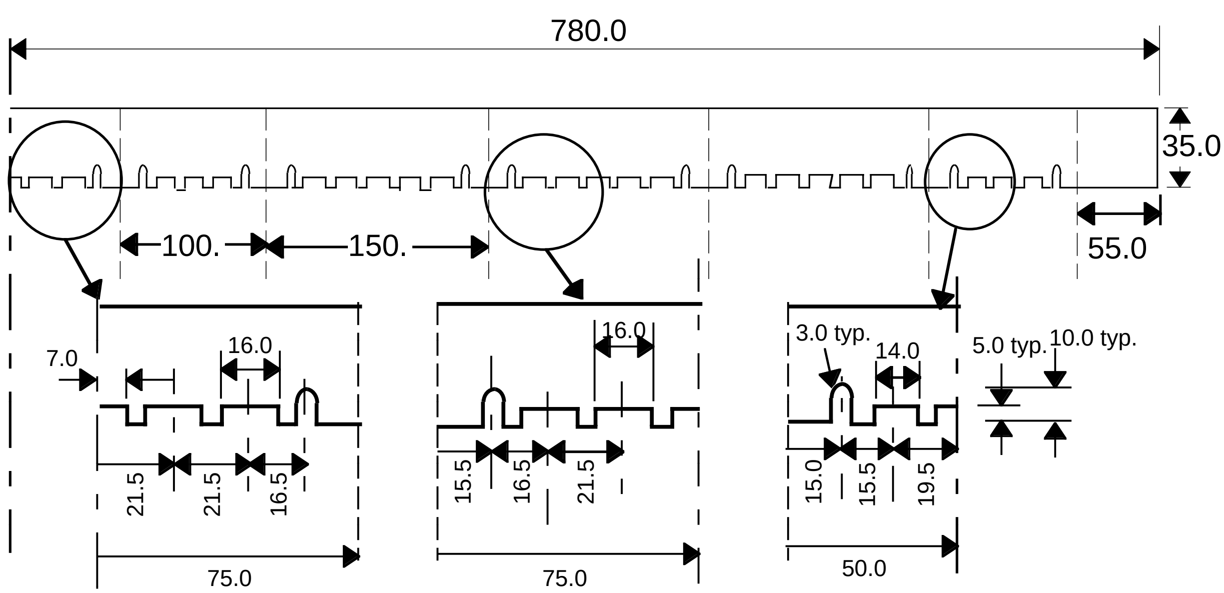

Figure 3 - Transverse section through half of wide face copper plate (new mold)

The submerged entry nozzle is a 3-port design with two large ports pointing towards the narrow faces and a small central port pointing downwards. The nozzle bore is 135 mm O.D. and 70 mm I.D. It tapers into a rectangular outlet region measuring 76 x 185 mm O.D. with 32 x 150

Modeling of Casting, Welding, and Advanced Solidification Processes VIII, B.G. Thomas and C. Beckermann, eds.,
(San Diego, CA, June 7-12, 1998), TMS, Warrendale, PA, 1998, pp. 1185-1199; [Best Experimental Paper Award, 1998, MCWASP VIII]

mm I.D. The nozzle is submerged about 130 mm below the steel / flux interface, measuring to the top of the large port. Further details on the nozzle and flow pattern are reported elsewhere [2].

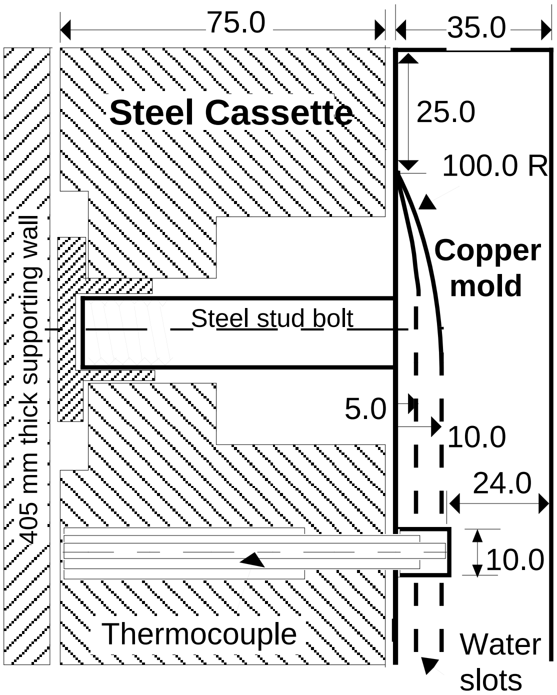

Figure 4 - Longitudinal section through new wide face copper plate and steel backing plate

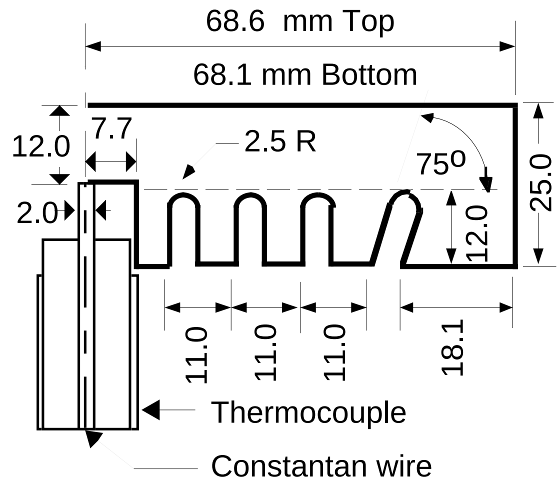

Figure 5 - Transverse section through narrow face copper plate at thermocouple (new mold)

Table 1. Mold Geometry

	Widefaces	Narrowfaces
Copper wall thickness	35.0 mm (new)	25.0 mm (new)
Total copper plate width	1560 mm	132.1 mm
Copper plate length	1200 mm	1200 mm
Distance between cooling water channels	21.5 mm	30.0 mm
Start of slots from mold top	25 mm	30 mm
Cooling water slot depth	5.0 mm (34 slots) 5.0 mm (13 slots) 10 mm (22 slots)	12 mm (8 slots)
Cooling water channel width	16.0 mm (34 slots) 14.0 mm (13 slots) 6.0 mm (22 slots)	5.0 mm (8 slots)
Channel cross sectional area	4865 mm^2 (each WF)	462.7 mm^2 (each NF)
Water flow rate	0.05677 m^3/s (IR) 0.05677 m^3/s (OR)	0.00631 m^3/s (East) 0.00631 m^3/s (West)
Cooling water velocity	11.67 m/s	13.64 m/s
Restraining bolts	11 across x 12 down (each WF)	12 studs (each NF center)

Modeling of Casting, Welding, and Advanced Solidification Processes VIII, B.G. Thomas and C. Beckermann, eds.,
(San Diego, CA, June 7-12, 1998), TMS, Warrendale, PA, 1998, pp. 1185-1199; [Best Experimental Paper Award, 1998, MCWASP VIII]

Breakout Shell Measurement

The breakout occurred while casting a 132 x 984 mm(5.2 x 38.75") slab of 434 stainless steel, under the generally steady conditions given in Table 2. The mold geometry is the same as the standard geometry (Table 1) except that all of the copper plates were machined back to only 24 mm thick at the time and the mold was not instrumented with thermocouples. The breakout occurred 48 minutes after changing from powder A to an exothermic powder, B, and 41 minutes after changing heats, although these events appeared to be unrelated to the breakout.

All of the powders in this study are fine-ground synthetic powders, whose properties are provided in Table 3. Table 3 also includes typical depths of the various layers, measured above the liquid pool using the steel and aluminum wire method. Note that the total depth of 35 - 58 mm was maintained by manual pushing and produces a "dark" surface. This is allowed to burn down to a red surface just before changing powders.

The breakout was caused by the opening of part of a long longitudinal crack. The hole itself is wedge-shaped, measuring 483 mm long and tapers to a maximum opening of 19 mm at the bottom. The hole extends from 965 to 1448 mm below the top of the shell and is 75 mm west of the center line down the inside radius wide face. The hole tapers into a longitudinal crack extending both upwards to within 300 mm of the meniscus, and downwards many meters below the breakout.

The mold oscillation practice includes a stroke of 5.13 mm at a frequency of 3.942 Hz, with 0.1 s negative strip time. Average oscillation mark depth and width were 0.4 +/-0.2 x 1.0 +/-0.5 mm, with a measured pitch of 7.1 +/-1 mm. The oscillation marks were generally well formed and horizontal, including near the breakout, indicating that lubrication conditions appeared to be normal. An anomalous surface feature is that the oscillation marks below the mold along the narrowface slant downwards toward the outside radius, as shown in Fig. 6. In addition, the narrow faces bulge outward about 30 mm each on the inside radius edges.

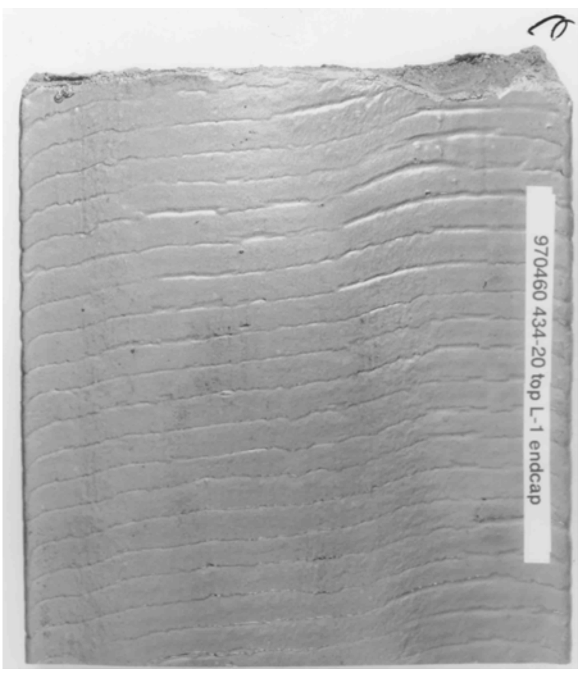

Figure 6 - Narrow face of breakout shell showing slanted oscillation marks (casting direction is downwards, inside radius is on right, section is 143mm long x 132mm thick)

Modeling of Casting, Welding, and Advanced Solidification Processes VIII, B.G. Thomas and C. Beckermann, eds.,
(San Diego, CA, June 7-12, 1998), TMS, Warrendale, PA, 1998, pp. 1185-1199; [Best Experimental Paper Award, 1998, MCWASP VIII]

Table 2. Casting Conditions:

		Steel Composition (434 Cr Steel)			
Casting speed	25.4 mm/s				
Strand thickness	132.1 mm	0.047	%C	0.10	%Cu
Strand width	984.0 mm	0.48	%Mn	0.008	%Sn
Tundish depth	990 mm	0.026	%P	0.0	%Ti
SEN submergence depth	127.0 mm	0.001	%S	0.003	%Al
Pour temperature	1563.0 ˚C	0.39	%Si	0.020	%Co
Meniscus dist. from mold top	104.0 mm	16.71	%Cr	0.026	%V
Mold conductivity	315.0 W/mK	0.20	%Ni	0.010	%Nb
Cooling water pressure	0.62 MPa	1.00	%Mo	0.056	%N

Table 3. Mold Powder and Flux Properties

	A	B	C
Powder Composition			
% SiO_2	29.4	33.8	38.4
% CaO	28.8	33.9	39.2
% Na_2O	9.3	10.6	2.0
% Fe_2O_3	11.0	0.3	0.7
% MgO	0.5	2.4	3.4
% Al_2O_3	6.6	6.2	5.0
% F	7.3	5.7	9.3
% S, % CO_2	-	-	0.6, 2.8
% other oxides			3.5
% C	6.0	4.1	2 .6
Flux Viscosity @ 1300 ˚C	1.4 Poise	2.3 Poise	2.0 Poise
Crystallization temp.	1140 ˚C	1146 ˚C	1135 ˚C
Powder layer depth	52 mm	18 mm	17 mm
Liquid layer depth	6 mm	17 mm	18 mm

Measurements of shell thickness were made along 14 different sections cut through the breakout shell, whose locations are indicated in Fig. 7. The measured profiles are given in the five frames of Fig. 8. Note that the portions of the shell near where the nozzle streams impinge (specifically the narrow faces and the off-corner regions of the wide faces) have generally slower shell growth, as expected.

Figure 9 plots several important variables as a function of time before and during the breakout. The stopper rod opening position is measured on a percent linear distance basis relative to an arbitrary initial reference point above the tundish well. Increasing the opening from 27% to 55% represents a roughly 3-fold increase in opening area and flow, from a steady value that is heavily throttled (mainly closed). Mold liquid level is determined by triangulating the signal from a radioactive source which is cut off at the average level of the molten steel. The liquid level recorded in Fig. 9 is relative to a horizontal line 260 mm below the top of the mold.

Modeling of Casting, Welding, and Advanced Solidification Processes VIII, B.G. Thomas and C. Beckermann, eds.,
(San Diego, CA, June 7-12, 1998), TMS, Warrendale, PA, 1998, pp. 1185-1199; [Best Experimental Paper Award, 1998, MCWASP VIII]

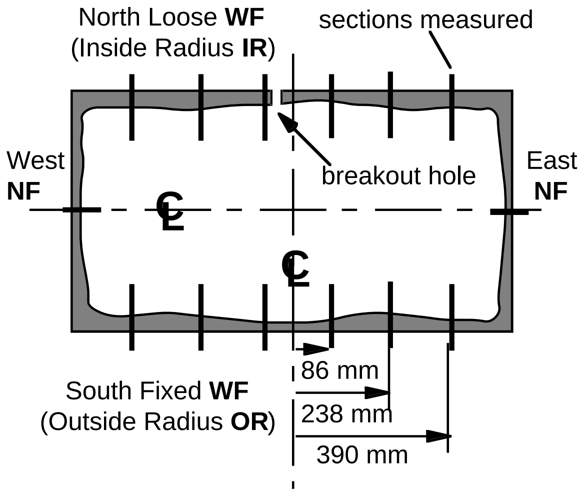

Figure 7 - Location of measured breakout shell sections around perimeter of mold

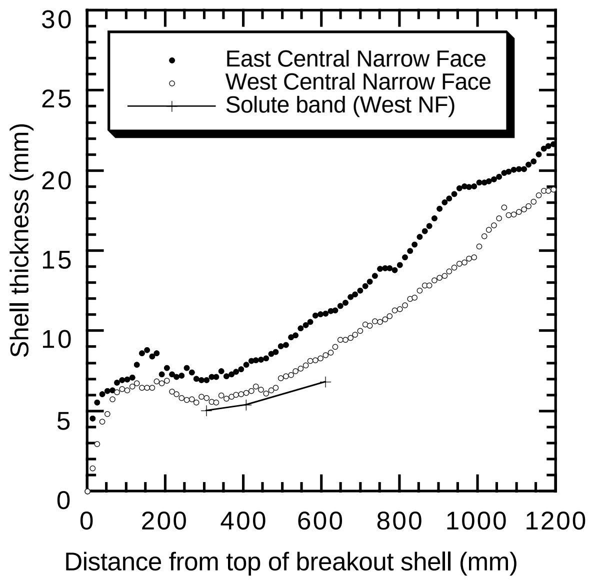

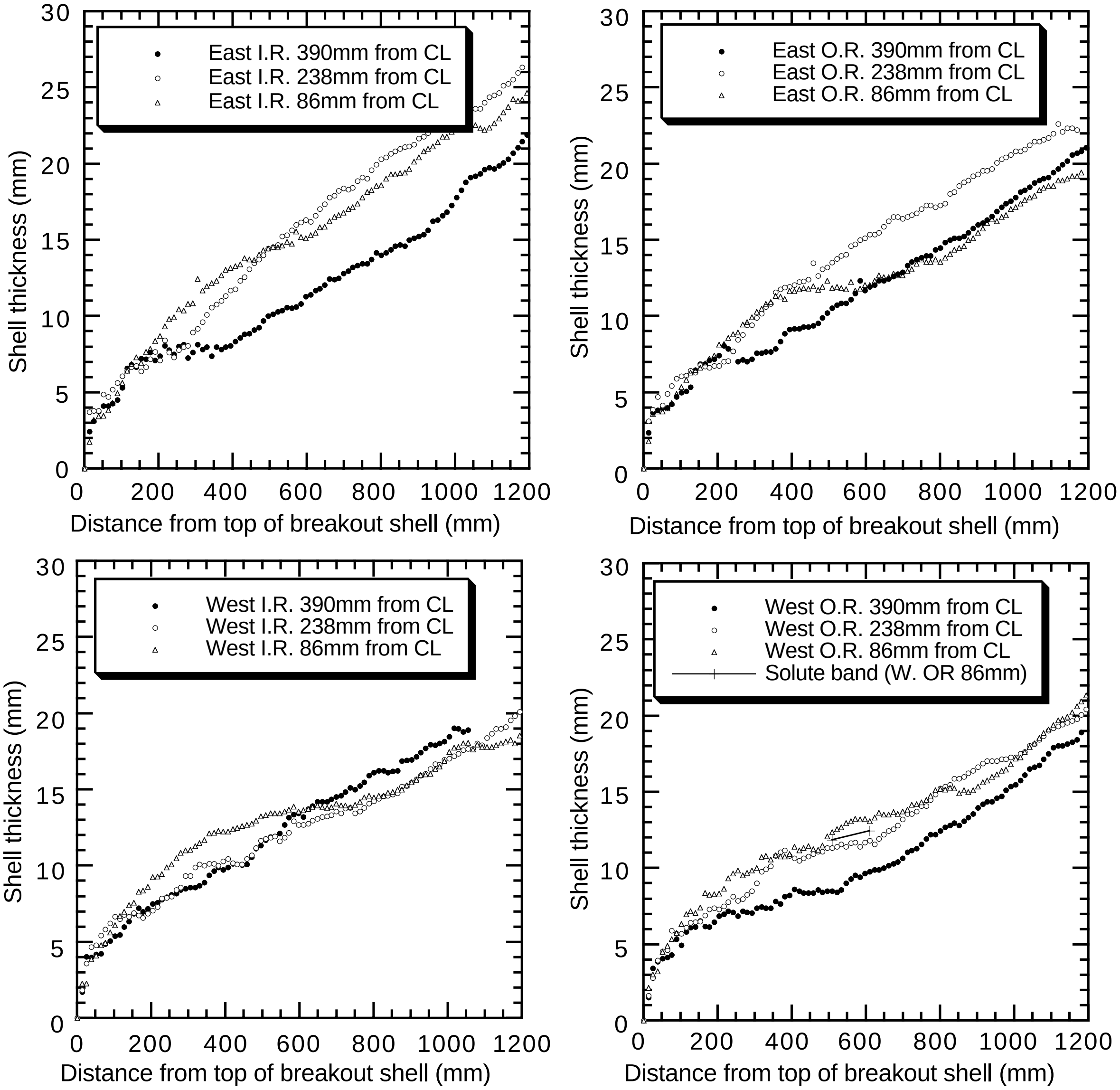

Figure 8 - Measured Breakout Shell Thickness profiles along 14 sections around mold perimeter

At the start of the breakout, 7178s, the drop in level was partially compensated by opening the stopper rod. Then after closing the stopper completely at 7190s, the level quickly dropped

Modeling of Casting, Welding, and Advanced Solidification Processes VIII, B.G. Thomas and C. Beckermann, eds.,
(San Diego, CA, June 7-12, 1998), TMS, Warrendale, PA, 1998, pp. 1185-1199; [Best Experimental Paper Award, 1998, MCWASP VIII]

beyond range of the sensor, so its subsequent signal is in error. Finally, casting was stopped completely at 7210 s.

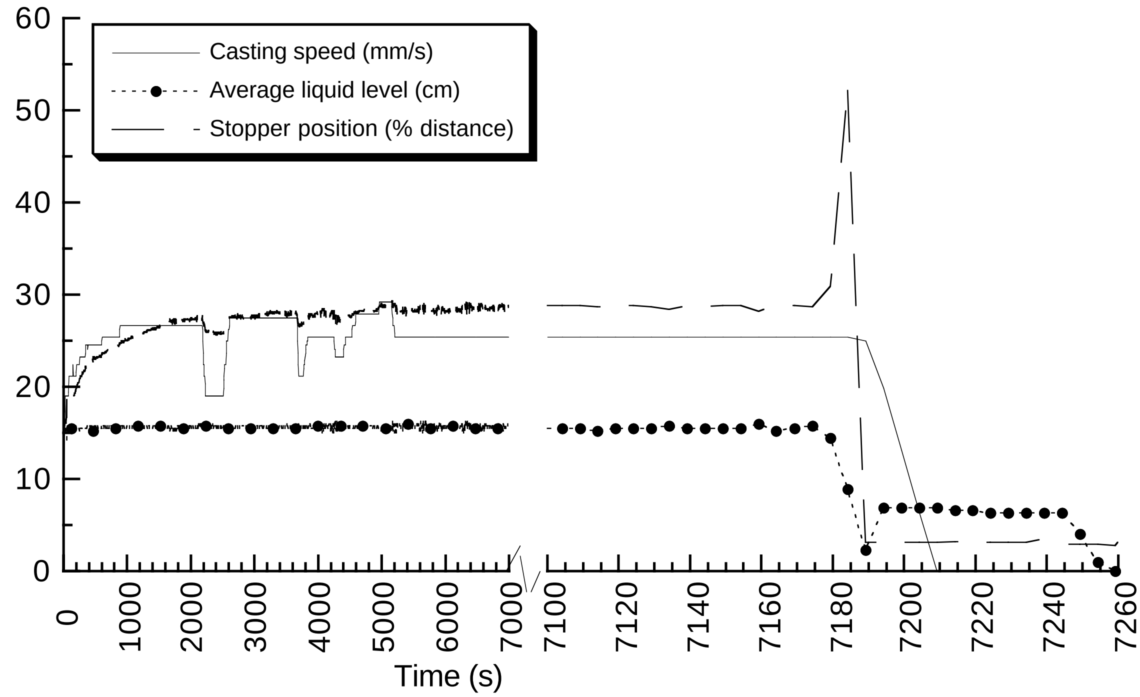

Figure 9 - History of recorded casting conditions with expanded scale during breakout

Figure 10 illustrates the movement of the shell during the breakout. Specifically, it presents distance versus time histories for several points on the strand surface, which eventually becomes the breakout shell. These curves were derived from the time-dependent casting-speed data in Fig. 9, by summing the instantaneous casting speed multiplied by the time increment, for different starting times. Zero distance corresponds to the position of the steady-state meniscus, normally held by the mold level controller at 104 mm below the top of the mold.

A reconstruction of the mold level history is presented on the same graph. The beginning of the curve is taken from the recorded data in Fig. 9. Beyond 7190s, the curve was extrapolated by estimating the drainage time, based on a 19x480 mm hole and initial head of 1450 mm [3].

Schematics of the breakout shell are superimposed on the graph at three critical times to illustrate the events during the breakout. The time when the level first starts dropping at 7178s indicates when the breakout hole first forms. Intersecting this time with the curve representing movement of the end of the breakout hole reveals that the breakout hole starts as a short hole just below the mold exit. The shell and hole both grow for the next 12s, as the input of new liquid partly compensates for the losses through the breakout hole. Then, at 7190s, the top of the final breakout shell forms, as the input flow of new steel stops and the shell drains. When withdrawal finally stops at 7210s, this point has traveled to 385 mm below the original liquid level position.

Because the shell drains fairly quickly, it is reasonably representative of steady casting conditions. For further accuracy, Fig. 10 can be used to obtain the solidification time for any point on the slab surface. Simply subtract the time a given point first drops below the liquid level (often at distance = 0) from the time the level later drops below its current position, as indicated by the intersection of the two curves. This information is included in Fig. 11, which magnifies the initial portion of a few shell thickness plots.

Modeling of Casting, Welding, and Advanced Solidification Processes VIII, B.G. Thomas and C. Beckermann, eds.,
(San Diego, CA, June 7-12, 1998), TMS, Warrendale, PA, 1998, pp. 1185-1199; [Best Experimental Paper Award, 1998, MCWASP VIII]

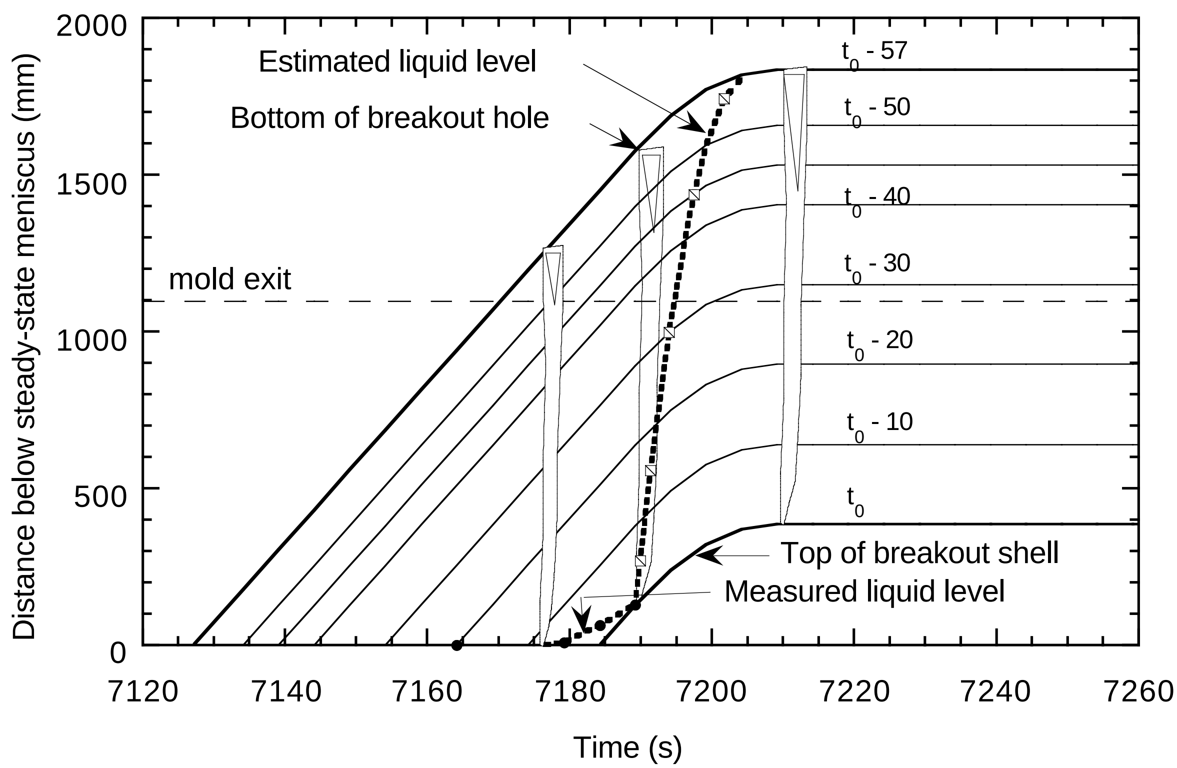

Figure 10 - Distance traveled by different points on the shell surface relative to the dropping liquid level

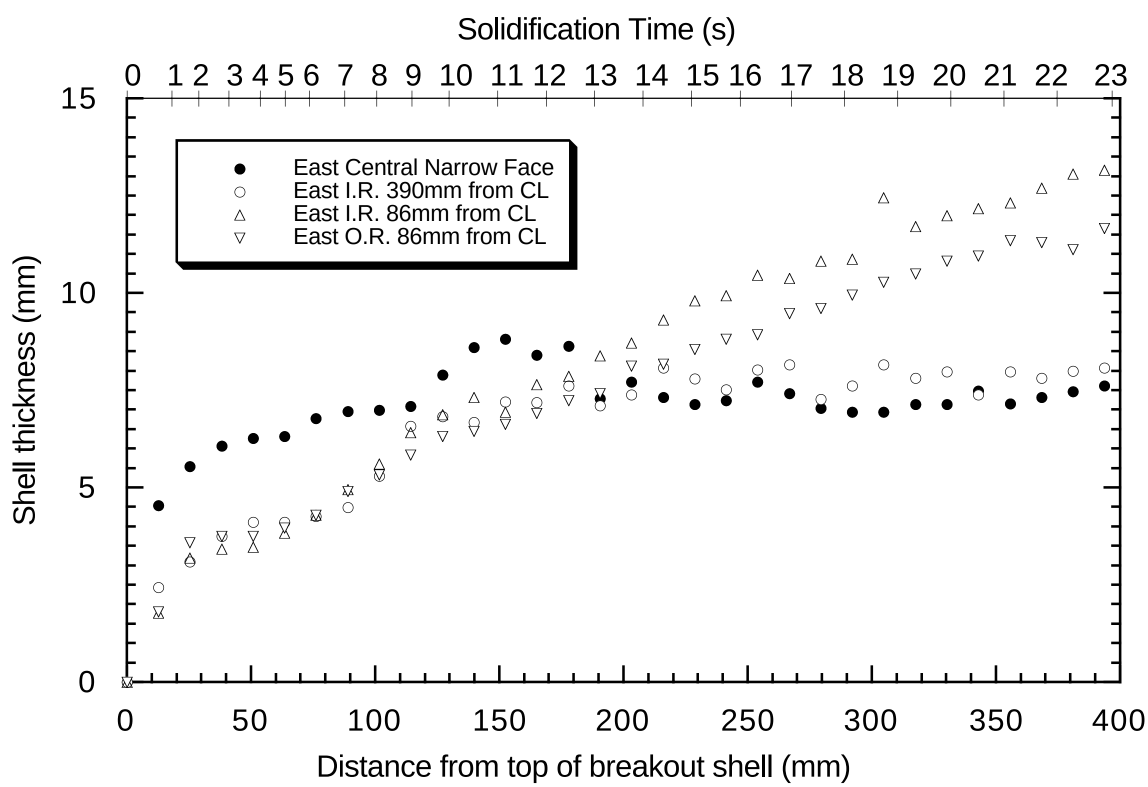

Figure 11 - Comparison of breakout initial shell growth profiles at various locations with corresponding solidification times

Modeling of Casting, Welding, and Advanced Solidification Processes VIII, B.G. Thomas and C. Beckermann, eds.,
(San Diego, CA, June 7-12, 1998), TMS, Warrendale, PA, 1998, pp. 1185-1199; [Best Experimental Paper Award, 1998, MCWASP VIII]

In general, the solidification time is almost directly proportional to distance along the breakout shell. However, this is not quite true at early times (less than 10s for this breakout). Initially, points on the breakout shell move downward faster than the level drops. Thus, the top of the breakout shell forms below the steady-state meniscus level. This portion of the shell is covered by molten steel longer than the initial portion of a shell cast under steady-state conditions would be. Thus, the distance between each second of solidification time in Fig. 11 is shorter at early times. This finding explains why model predictions of the steady-state shell thickness might underpredict the breakout shell thickness near the meniscus. Models based on matching the local solidification time should match the breakout shell profile more readily.

Figure 11 shows that drainage through the breakout hole did not appear to have much influence on shell growth, as shell growth beside the breakout hole is similar to that across the mold on the outer radius. Shell growth at both the narrow face and off-corner of the wideface are generally reduced relative to the central regions of the wide face. This is likely due to superheat from the impingement of the strong jets which flow from the nozzle ports and expand as they traverse across the mold. The east side is a generally a little thicker than the west side, for reasons unknown.

Temperature Measurement

<u>During Breakout</u>

The mold which experienced the breakout was not instrumented, so copper temperatures were not recorded. Figure 12 shows the water temperatures recorded before and during the breakout. The water inlet temperature remained fairly steady at about 35˚C during the breakout events. The outlet temperature was about 8˚C higher, with the exact temperature increase plotted in Fig. 12. This data can be used to perform a global heat balance on the mold. Care must be taken to consider that the temperature differences are measured for all of the water flowing through the mold, including water flowing through slots that were not adjacent to molten steel, owing to the narrow strand width.

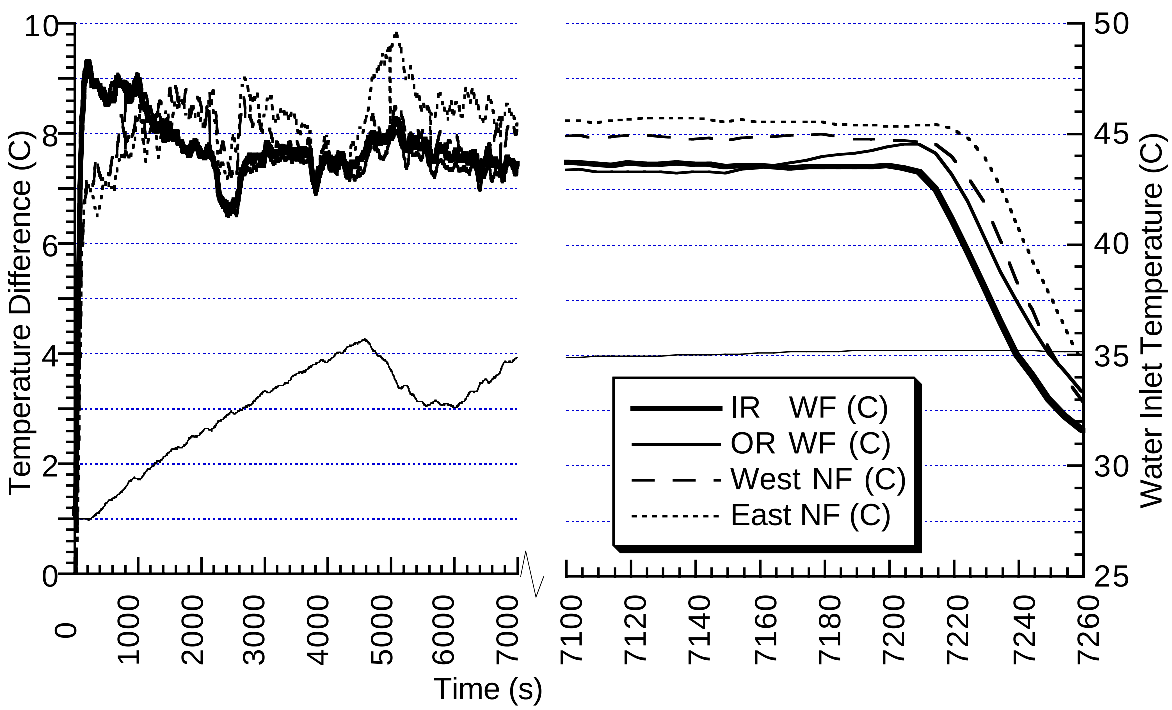

Figure 12 - History of mold cooling water temperature (with expanded scale during breakout)

Modeling of Casting, Welding, and Advanced Solidification Processes VIII, B.G. Thomas and C. Beckermann, eds.,
(San Diego, CA, June 7-12, 1998), TMS, Warrendale, PA, 1998, pp. 1185-1199; [Best Experimental Paper Award, 1998, MCWASP VIII]

An instrumented mold containing 106 thermocouples was used to obtain typical temperatures during steady casting conditions similar to those just prior to the breakout. The mold geometry is the same as given in Table 1, as the mold was new. Casting conditions are the same as the breakout conditions (Table 2), except that powder C was used (Table 3).

The location of each thermocouple is given in Fig. 13. Thermocouples were aligned vertically between the bolt holes and extended to 24 mm below the wide face copper hot face and 12 mm below the narrow face according to the design given in Figs. 3-5.

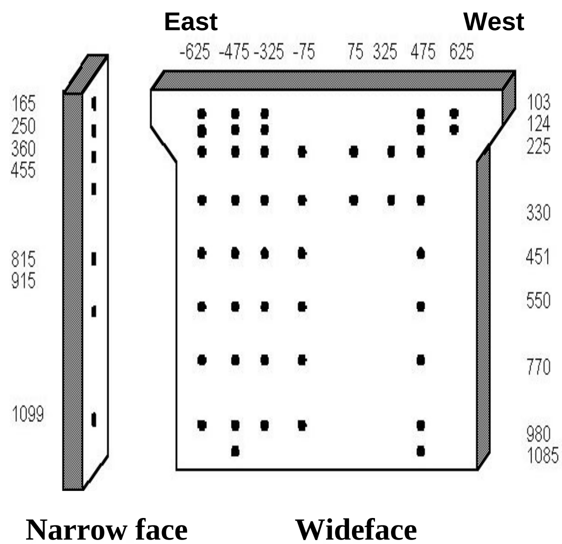

Figure 13 - Location of thermocouples on narrow and wide faces. (Distances in mm are measured below the top of the mold and across the wide face relative to the centerline.)

Each thermocouple consists of a 2-mm diameter constantan wire or "stud" which is welded to the bottom of its inset hole in the back of the copper plate. The copper mold itself serves as the copper portion of the thermocouple junction. To keep water out of the inset hole, the constantan wire is sheathed with an insulating plastic plug.

Measured mold cooling water temperature differences averaged: 7.44 ˚C (IR), 7.45 ˚C (OR), 7.93 ˚C (West NF) and 8.05 ˚C (East NF).

Figure 14 presents the measured temperatures for 86 thermocouples, (excluding the 625 mm columns). The location of each thermocouple is indicated by its distance from the centerline and below the top of the mold, corresponding to Fig. 13. Error bars indicate the average range of fluctuations observed in each reading over time. The lines in Fig. 14 are only to help identify the points. Near the meniscus, the actual mold temperature between the measured points is expected to be much higher. A vertical arrow indicates the estimated location of the maximum mold temperature, which is about 40 mm below the liquid level.

Note that wideface temperatures near to the narrow faces (475 mm) are consistently lower on both the inside radius (IR) and outside radius (OR). The narrow faces consistently record the highest temperatures.

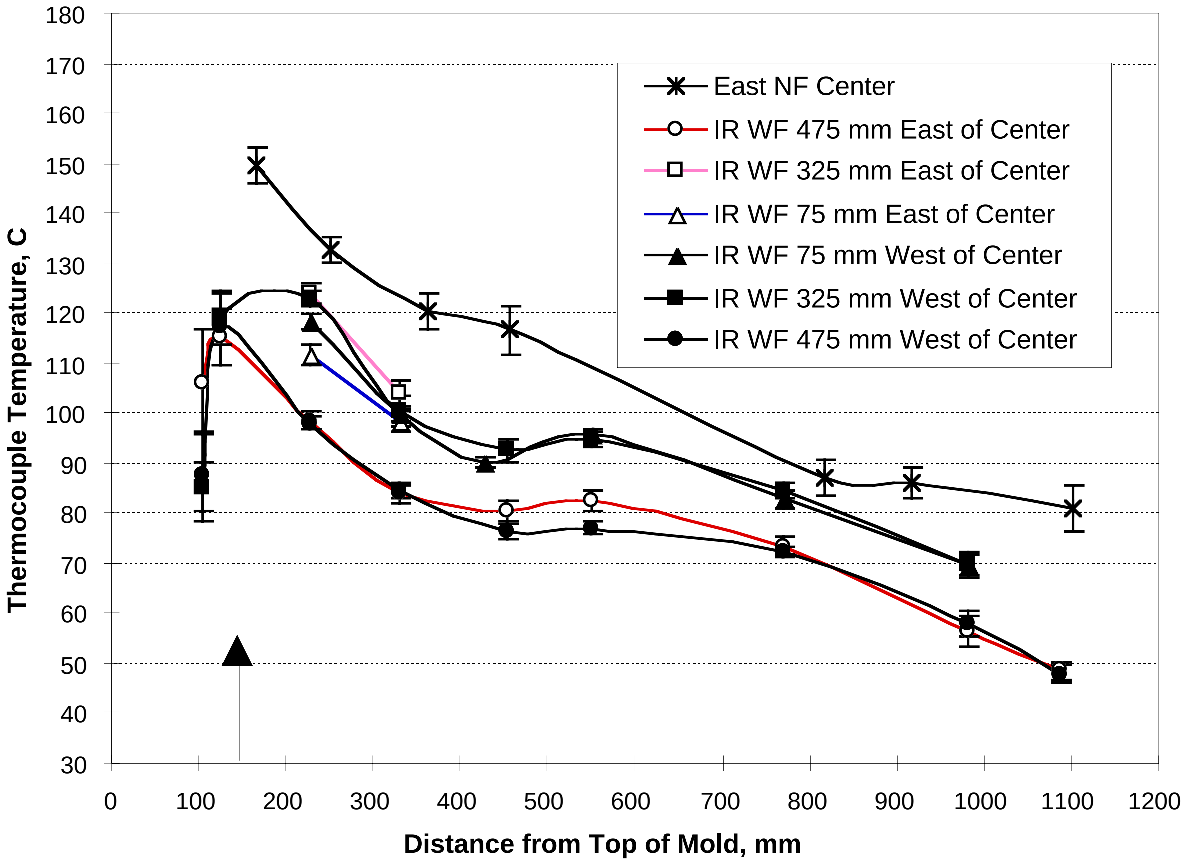

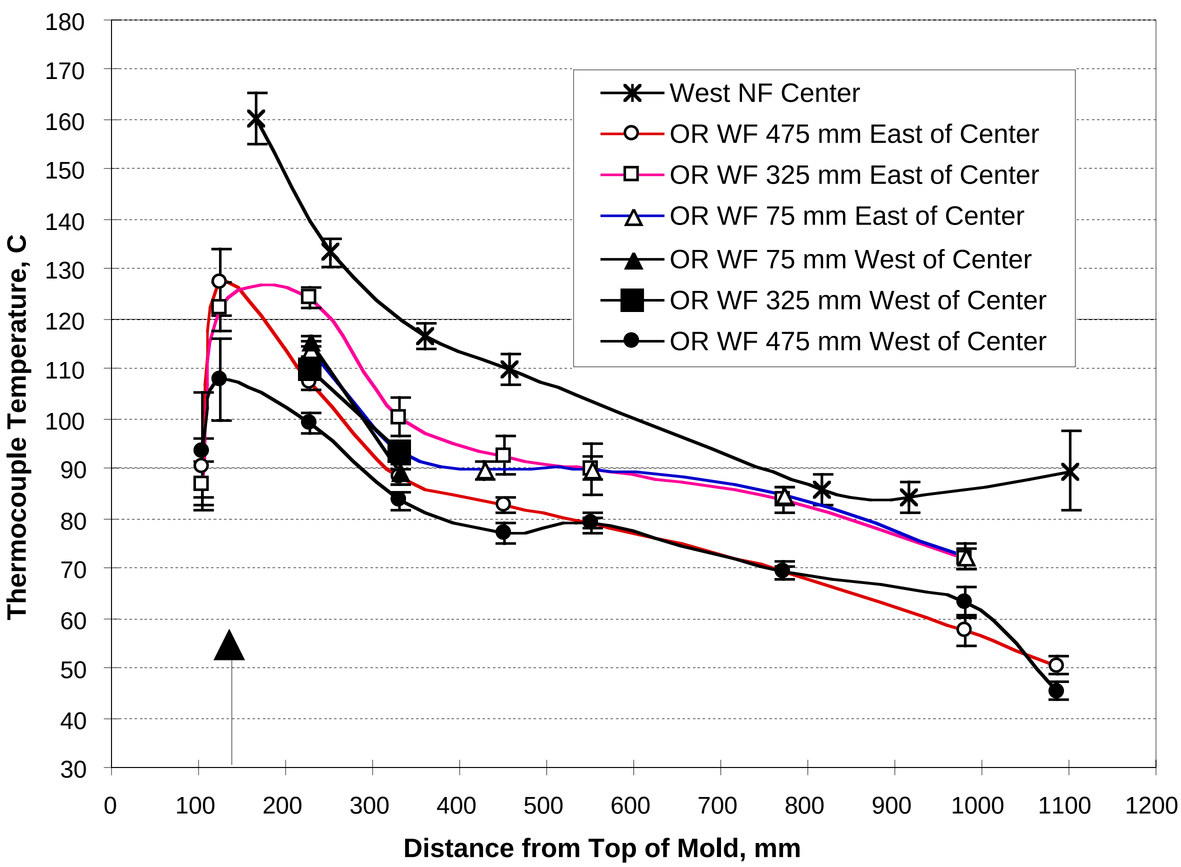

Figure 14 - Mold temperatures

Modeling of Casting, Welding, and Advanced Solidification Processes VIII, B.G. Thomas and C. Beckermann, eds.,
(San Diego, CA, June 7-12, 1998), TMS, Warrendale, PA, 1998, pp. 1185-1199; [Best Experimental Paper Award, 1998, MCWASP VIII]

Microstructure Investigation

Metallographic analysis was performed on samples taken from the breakout shell and from the solid strand just below. Measurements were performed to determine the dendrite arm spacings and final columnar grain size.

Dendritic Structure and Arm Spacings

Figures 15 and 16 show the dendritic structure in longitudinal sections taken at two different distances below the top of the breakout shell, through the center of the west narrow face. The dendritic structure was revealed using about 45s immersion in a solution of 10 g $CuCl_2$ in 50 ml HCl, 50 ml C_2H_5OH and 100 ml H_2O [4].

Figure 15 shows the microstructure between 8 and 10 mm below the top of the narrow face of the breakout shell, where the shell is only 1.00 mm thick. The secondary arm spacing is about 18 μm, and is relatively uniform across the sample. The corresponding primary arm spacing is variable, but averages 46 μm.

Figure 16 shows the microstructure taken 813 mm below the top of the narrow face of the breakout shell, where the shell is 11 mm thick. A close-up taken near the drained interface is shown. The secondary arm spacing is about 40 μm and the primary spacing is 127 μm. Note that the dendrites angle slightly upwards (opposite to the casting direction). The small white regions are carbide precipitates.

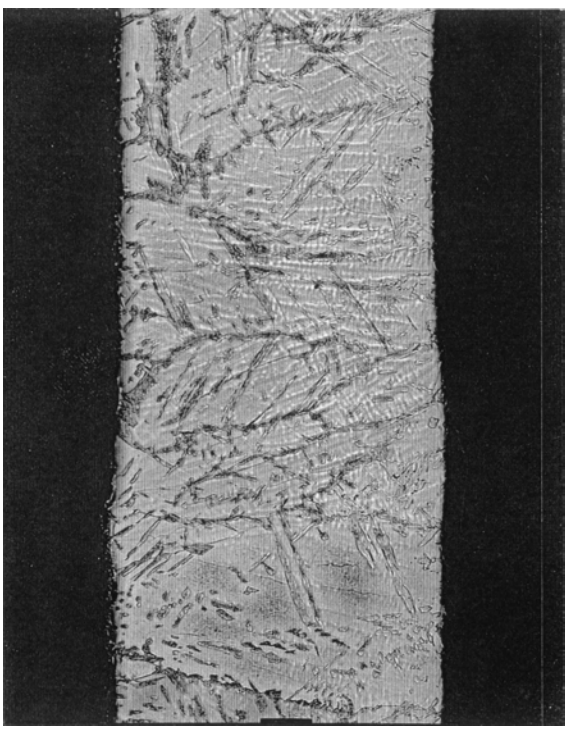

Figure 15 - Dendritic structure near top of NF breakout shell. The total thickness from the strand surface (right) to the drained interface (left) is 1.00 mm at the bottom

Figure 17 shows the increase in primary and secondary dendrite arm spacings measured down the breakout shell near the narrowface and wideface centerlines. All measurements were made near the drained interface. The dip in primary spacing along the narrow face appears to correspond with the point of jet impingement that causes the dip in shell growth at about the same distance.

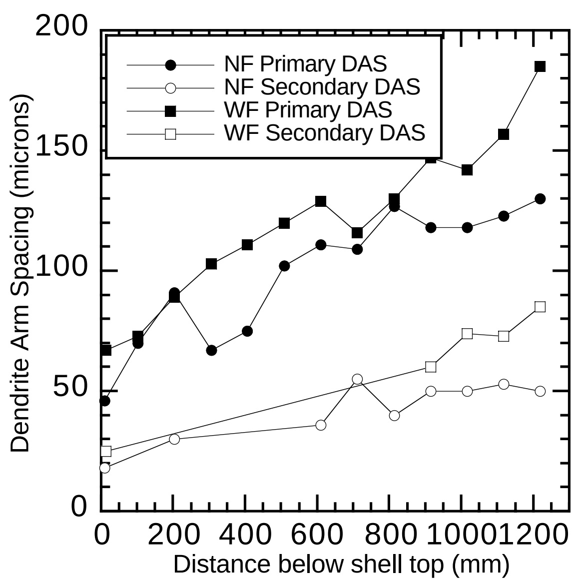

Figure 17 - Measured dendrite arm spacings for different distances down narrow and wide face of breakout shell

Modeling of Casting, Welding, and Advanced Solidification Processes VIII, B.G. Thomas and C. Beckermann, eds.,
(San Diego, CA, June 7-12, 1998), TMS, Warrendale, PA, 1998, pp. 1185-1199; [Best Experimental Paper Award, 1998, MCWASP VIII]

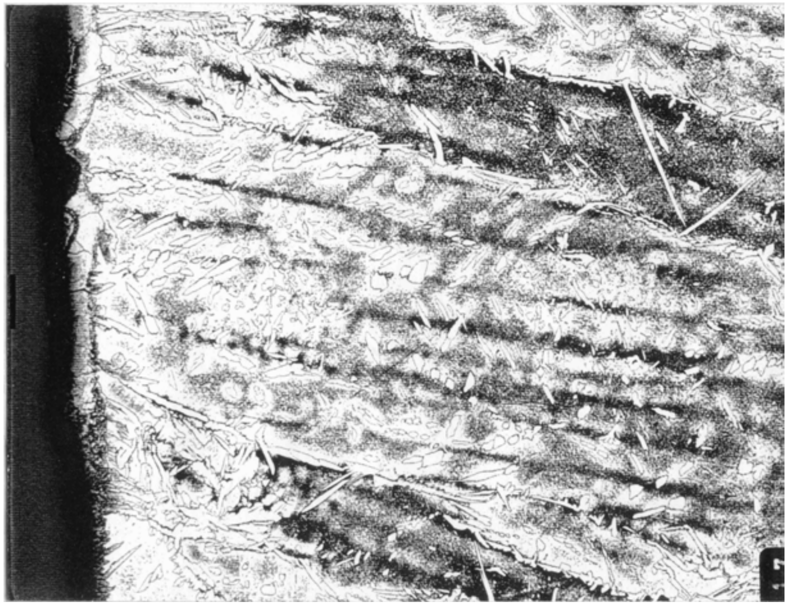

Figure 16 - Dendritic structure 813 mm below top of west NF breakout shell near the drained interface (left). Only 2.15 mm of the total 11 mm thickness is shown (same scale as Fig. 15) Casting direction is downward.

Grain Structure

Sample sections were etched to reveal the columnar grain structure in a representative region of the slab. Macro-etching was performed using Villellas's etchant.

Figure 18 presents a horizontal section through the strand, from the west narrow face to the wide face centerline, and including the longitudinal crack that later started the breakout. This section was taken 127m below the top of the breakout shell, where casting conditions were reasonably typical of steady state. Anomalous features are the longitudinal crack, and corresponding bulging of the narrow face inside radius. The crack is 32 mm deep and 10 mm wide at the surface of this section. Note that the final grain structure, shown in Fig. 18, is almost 100% columnar. Most of the structure consists of grains which span across half the strand thickness, making them 65 mm long. Their width varies from 2 to 7 mm.

Figure 19 presents the macrostructure of a typical longitudinal section at about the same distance below the top of the breakout shell. This section was taken near to the east narrow face, (25 mm from the OR corner and 38 mm from the bulged IR corner). Because it is so near to the narrow face, the section cuts through columnar grains that are growing away from the narrow face, so are oriented perpendicular to the section. Thus, these grains appear equiaxed in this view, even though they are actually all columnar. Their average diameter is about 1.5 mm. Note that the columnar grains that initially grow inward from the wide faces, slant slightly downward (in the casting direction). Then, at about 7 mm from the surface, they turn to slant in the opposite direction (upward) with further growth. This is consistent with growth slanted towards the flow direction, considering the changing direction of flow experienced by this portion of the shell.

Solute Bands

In several micrographs, intermittent dark bands of enriched solute traverse across the dendrites, roughly parallel to the solidification front. They were observed only at locations near the drained interface where the liquid jet likely impinges directly on the shell. As shown in Fig. 8, they are 0.75-1.64mm beneath this interface on the narrowface centerline (0.57mm beneath the wideface) and extend from 305-610mm below the meniscus along the NF (508-610mm down the WF).

Conclusions

Measurements have been made to quantify a particular set of typical process conditions for the continuous casting of stainless steel slabs at Armco, Inc. in Mansfield, OH, focusing on the analysis of a breakout shell. The data include shell thickness, mold temperature, and microstructure measurements. The breakout appears to be representative of normal casting conditions and information is provided to allow all of the data to be used together in order to validate mathematical models of the process.

Modeling of Casting, Welding, and Advanced Solidification Processes VIII, B.G. Thomas and C. Beckermann, eds.,
(San Diego, CA, June 7-12, 1998), TMS, Warrendale, PA, 1998, pp. 1185-1199; [Best Experimental Paper Award, 1998, MCWASP VIII]

Figure 18 - Columnar grain structure in a transverse section through the strand, far below the breakout hole. Note the deep longitudinal crack which later caused the breakout (lower right) and the bulging on the inside radius narrow face (top right)

Figure 19 - Longitudinal section parallel to east narrow face (casting direction downward; inside radius on left)

References

1. B.G. Thomas, D. Lui & B. Ho, in Applications of Sensors in Materials Processing, V. Viswanathan, ed., (TMS, Warrendale, PA: Orlando, FL, 1997), 117-142.
2. P. Gittler and M. Brummayer, “Numerische Simulation der Stromungsverhaltnisse in Einer Kikille” (Report, Johannes Kepler Universitat, Linz, Austria, 1997).
3. A. Moitra and B.G. Thomas, in Steelmaking Proceedings, 76, (Iron and Steel Society: Dallas, TX, 1993), 657-667.
4. B. Callmer and O. Grinder, Scand. J. Metallurgy, 9 (1980).

Modeling of Casting, Welding, and Advanced Solidification Processes VIII, B.G. Thomas and C. Beckermann, eds.,
(San Diego, CA, June 7-12, 1998), TMS, Warrendale, PA, 1998, pp. 1185-1199; [Best Experimental Paper Award, 1998, MCWASP VIII]

Acknowledgments

The authors wish to thank the Continuous Casting Consortium at UIUC, including AK Steel, (Middletown, OH), Allegheny Ludlum, (Brackenridge, PA), Armco Inc. (Middletown, OH), Inland Steel Corp. (East Chicago, IN), LTV (Cleveland, OH), and Stollberg, Inc., (Niagara Falls, NY) for their continued support of our research and the National Center for Supercomputing Applications (NCSA) at the UIUC for computing time. Additional thanks are extended to technicians at Armco, Inc. for help preparing and measuring samples.

Corrections to water temperature increase results for global heat balance:

cooling water temperature reads a value or "bias" (eg. 1.38˚C) when no steel is flowing!
so, should subtract 1.38 from cooling water delta-T to get true delta-T

Standard (steady) conditions

Mold Face	Measured ΔT	Bias	True ΔT
Inside Radius	7.44 C	1.38	6.06 C
Outside Radius	7.45 C	1.27	6.18 C
West Narrow	7.93 C	0.04	7.89 C
East Narrow	8.05 C	-0.02	8.07 C

Breakout conditions

Mold Face	Measured ΔT	Bias	True ΔT
Inside Radius	7.28 C	1.14	6.14 C
Outside Radius	7.46 C	1.03	6.43 C
West Narrow	7.87 C	-0.21	8.08 C
East Narrow	8.20 C	-0.28	8.48 C

the apparent brief increase in mold level after the breakout occurs is an anomolous reading due to the empty SEN blocking the detector when it is moved out of the way.

References dealing with deflecting dendrites.

- 1. "Improvements of slab quality with in-mold electromagnetic stirrer", Jun Fukuda et al., Proceedings of 3rd European Conference on Continuous Casting, Madrid Spain, 1998, pp. 437-445. (This ref. refers to an older reference, S. Okano et al., Tetsu-to-Hagane, Vol. 61 (1975), pp. 2982.)
- 2. "Numerical Modeling of Deflected Columnar Dendritic Grains Solidified in a Flowinf Melt and Its Experimental Verification", S. Y. Lee, S. M. Lee and C. P. Hong, ISIJ International, Vol 40 (2000) No. 1, pp. 48-57.